

Explicit Topology Optimization of Voronoi Foams

Ming Li, Jingqiao Hu, Wei Chen, Weipeng Kong, and Jin Huang

Abstract—Topology optimization can maximally leverage the high DOFs and mechanical potentiality of porous foams but faces challenges in adapting to free-form outer shapes, maintaining full connectivity between adjacent foam cells, and achieving high simulation accuracy. Utilizing the concept of Voronoi tessellation may help overcome the challenges owing to its distinguished properties on highly flexible topology, natural edge connectivity, and easy shape conforming. However, a variational optimization of the so-called Voronoi foams has not yet been fully explored. In addressing the issue, a concept of explicit topology optimization of open-cell Voronoi foams is proposed that can efficiently and reliably guide the foam’s topology and geometry variations under critical physical and geometric requirements. Taking the site (or seed) positions and beam radii as the DOFs, we explore the differentiability of the open-cell Voronoi foams w.r.t. its seed locations, and propose a highly efficient local finite difference method to estimate the derivatives. During the gradient-based optimization, the foam topology can change freely, and some seeds may even be pushed out of shape, which greatly alleviates the challenges of prescribing a fixed underlying grid. The foam’s mechanical property is also computed with a much-improved efficiency by an order of magnitude, in comparison with benchmark FEM, via a new material-aware numerical coarsening method on its highly heterogeneous density field counterpart. We show the improved performance of our Voronoi foam in comparison with classical topology optimization approaches and demonstrate its advantages in various settings.

Index Terms—Topology optimization, microstructures, Voronoi foams, 3D printing, full connectivity, high simulation accuracy.

I. INTRODUCTION

POROUS foams have attractive and distinguishing properties of lightweight, high stiffness-ratio, energy absorption, flexibly tailored rigidity and so on [1]–[4]. Topology optimization is very effective in maximally leveraging the high DOFs and mechanical potentiality of porous foams [5], [6], in constructing the optimized cell configurations and cell distribution within the design domain.

However, most of the previous topology optimization approaches were built up on voxel-like structure: the foams are described via voxel density distributions, specific porous cells are distributed (nearly) periodically within a prescribed axis-aligned regular grid, and the simulation and optimization are conducted with the regular grid [5], [6]. These simplify modeling, simulation, and optimization, but also restrict the topology optimization’s potential in tightly adapting to a free-form outer shape, reliably maintaining full connectivity between adjacent cells, and convincingly predicting the foam’s physical properties. Novel topology optimization approaches are in high demand to resolve these issues.

On the other hand, utilizing the concept of Voronoi tessellation for porous foam design seems very promising [7],

[8]. We particularly focus on open-cell foams in this study as their open interior allows for ease of material clearance after fabrication; natural open-cell foams are often idealized as edges of Voronoi cells [9]. This Voronoi-based foam representation naturally inherits many merits from the Voronoi diagram. For instance, the conventional density-based topology optimization may lead to dangling parts after thresholding, and this limitation can be easily resolved by this representation because the edges of the Voronoi diagram are always connected (if no additional clipping). Besides, the relationship between seeds and edges in Voronoi diagram is localized, which helps develop efficient optimization algorithm. We clip the result from the unconstrained Voronoi diagram by an input free-form surface, which results in a foam structure tightly adapting to the input shape following a similar strategy in [7].

However, the extensive topology variations of Voronoi foams have not been much explored – conducting a reliable and efficient topology optimization of open-cell Voronoi foams to meet critical physical requirements is still a challenging task. Although being widely explored, most previous approaches on Voronoi foam design tended to fix the number (or density) of the seeds, even their locations, and could not optimize it w.r.t. mechanical goal in a variational way [7], [10]–[13]. The recent excellent work of Lu et al. [14] and Feng et al. [15] only focused on the topology optimization of *close-cell* foams in 3D; differences between these approaches are to be detailed in Section II-C.

In this study, we develop an *explicit topology optimization* to construct an open-cell foam of optimized mechanical performance, under clear topology and geometry control parameters, using the site (or seed) positions and beam radii; See also Fig. 1. It has the following main contributions:

- 1) We provide explicit control parameters with extensive design space to simultaneously optimize a foam’s topology and geometry, always resulting in a free-form foam of full connectivity inside of the object. The approach is also able to tune the foam cell number automatically, which was seldom observed in previous studies of biscale-topology optimization or cell-tiling-based optimization.
- 2) We simulate with high accuracy the deformation of the extremely complicated porous foams by a numerical coarsening approach. It solves the equilibrium equation about its high-resolution heterogeneous density field without the assumption of scale separation and reduces the computational costs by an order of magnitude compared with benchmark FEM results.
- 3) We explore deeply the differentiability of 3D open-cell Voronoi foams w.r.t. its seed locations, and the associated gradient-based topology optimization framework. The gradient is computed via a local finite difference approach, without efforts of expensive Voronoi construction,

The authors are with State Key Laboratory of CAD&CG, Zhejiang University, Hangzhou, 310027, China. E-mail: {liming, hj}@cad.zju.edu.cn, {hujingqiao, chen_w, wpkong}@zju.edu.cn.

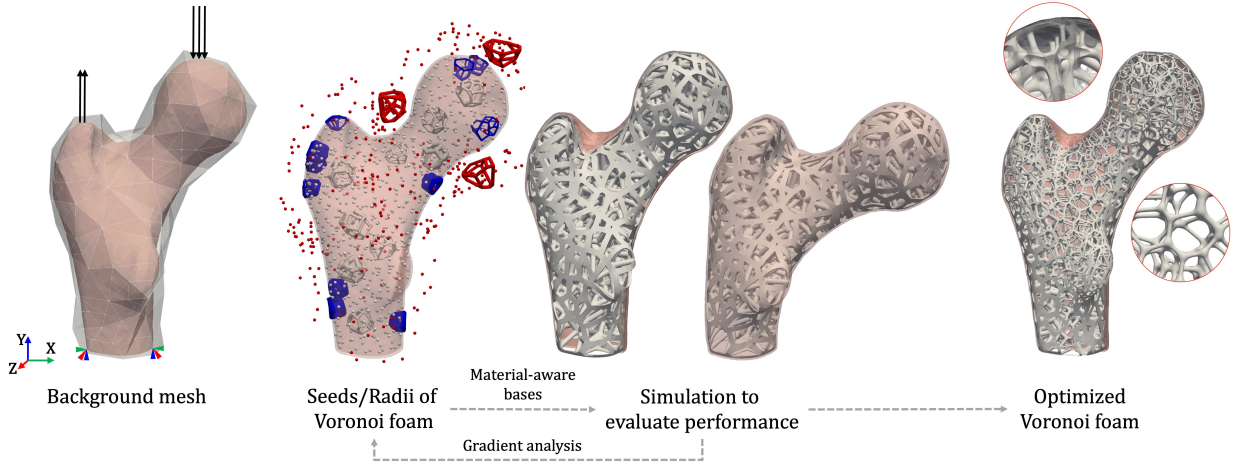


Fig. 1. The procedure of explicit topology optimization. The domain is first embedded within a coarse background mesh. Then, starting from an initial Voronoi foam described by the design variables of seeds and radii, the foam is efficiently simulated using material-aware coarsened bases and repeatedly updated by the gradient computations. The final optimized Voronoi foam is shown on the rightmost.

and significantly improves the efficiency.

- 4) We devise a synchronized explicit and implicit foam representation for topology optimization of conforming Voronoi foams. It forms a seamless pipeline that conducts the modeling, simulation, and gradient computation on a uniform implicit representation, avoiding the unstable and time-consuming model conversions between modeling and simulation.

The proposed approach applies to a wide range of physics-based porous foam optimization. We specifically focus on a widely studied stiffness maximization for proof of concept, and also for representative performance comparisons.

The remainder of the study is arranged as follows. Related work is discussed in Section II. The idea and overview of the Voronoi foam optimization is explained in Section III. After a problem formulation in Section IV, approaches on the optimization and simulation are explained in Sections V and VI. Extensive numerical examples are given in Section VII, followed by the conclusion in Section VIII.

II. RELATED WORK

We discuss the related work on simulation, optimization of porous foams, and the free-form foam design.

A. Foam simulations

The property of a porous foam can be directly predicted using the classical FE method by tessellating it into a discrete volume mesh. However, its geometric structure is too complicated which poses severe challenges to its reliable FE mesh generation and efficient solution computation.

Typically, a foam is simulated via numerical homogenization [16], [17]. It is achieved via two levels of FE computations - coarse-level and fine-level wherein the simulation results on each foam cell are used in parallel to predict the overall performance in the coarse-level, and vice versa. The approach replaces each foam cell with an effective elasticity tensor via the asymptotic [18] or energy-based approximations [17],

assuming scale separation and periodic cell distribution. In contrast, the Voronoi foams studied here have *cutout or full-solid covering shells*, which seriously breaks the assumption. Applying directly these approaches may reduce the simulation accuracy. The reduced order model (ROM) was recently proposed to simulate the porous foams [19]. It shares the same spirit with the approach in representing the shape function as a matrix transformation [20]. Yet it is designed for lattice structures consisting of well-defined unit cells and is not directly applicable for the studied Voronoi foam. Note that it is not very reasonable to simulate our foam as an assembly of *beam elements* [21] as the foam involves smooth blends between the beams or even covering solid shells.

Being embedded within a coarse background mesh, a porous foam can be taken as a heterogeneous structure and simulated via numerical coarsening with no assumption of scale separation [22], [23]. We here construct material-aware shape (or “basis”) functions to reflect finely the material distribution within each coarse element, which has shown great potential in improving the simulation effectiveness of heterogeneous structures [24], [25]. Weighted piecewise-trilinear shape functions were initially introduced [24]. Later on matrix-valued form was devised to capture the complicated non-linear and anisotropic stress-strain behavior with an improved accuracy [25], achieved via solving a relatively expensive optimization problem. Very recently, the shape functions in an explicit form of matrix product were introduced [20], which overcomes the challenging issue of inter-element stiffness and ensures the fine-mesh solution continuity. We further extend the approach in this study to simulate Voronoi foams on general background polyhedral meshes. The approaches share a similar spirit with the finite cell method (FCM) [26] using higher-order FE shape functions on a background mesh.

B. Foam optimizations

Optimization of porous foams has been widely studied via topology optimization or parametric optimization [5], [6]. The topology optimization is conducted separately in a single

scale or concurrently in a biscale optimization [27]–[31]. When in a single scale, it requires imposing local volume constraints to generate bone-like foams [30], or constraints of solid and void sizes [32], [33]. These constraints were tediously designed manually and raised additional difficulty in its optimization convergence. Strategy using stress trajectory guided density initialization [34], [35] was proposed to resolve the convergence issue. More recently, Hu et al. [36] developed porous thin-shell structures by engraving patterns on thin-shell structures and optimizing the pattern parameters (e.g. size and orientation). When in biscale, maintaining the geometric connection between adjacent cells comes out as a fundamental challenge. Huge research efforts have been devoted to resolving them [27], [37]–[39], but they have no effective shape control ability due to the intrinsic low-level voxel-based shape representations. Geometrically invalid structures were usually found in the optimized structures that may contain broken, slender, or small-void regions; see the examples in Section VII-B. The recent approach of MMC (Moving Morphing Components) [40] conducted the topology optimization using simple geometric primitives, which shares the same spirit of the study.

Utilizing fixed types of parametric cells for foam optimization has also been studied. The cell parameter distribution was optimized for improved performance or to follow certain material properties or stress directions [41]–[44]. Various types of cells were explored, for planar rod networks [45], for strongly controlled anisotropy [46], or based on TPMS (Triply Periodic Minimal Surfaces) [47], [48]. Tozoni et al. [49] optimized rhombic family for irregular foams conforming to an arbitrary outer shape. These approaches have ease in generating foams of full connectivity, at a cost of limited design choices. Great efforts have been devoted to extending the cell types via de-homogenization [17], [27], [41], [50].

C. Free-form foam design

Most of the above approaches work on a regular grid within a biscale framework linking the design domain and the foam cells. Their extensions to free-form shapes are generally achieved in three different ways: (1) assuming a sufficiently fine cell size and ignoring the cell-shape gap; (2) via cell clipping which may destroy the integrity of the boundary cells [7]; (3) deforming foam cells to fit in a conforming hexahedral mesh [49], [51]–[53], where the cells may be extremely deformed. Recently, Wu et al. [31] proposed an excellent approach of conforming foam design in consecutive steps of material optimization and conforming foam generation. TPMS, as a special type of foam, can naturally maintain full connectivity after boolean operations with outer shapes [47], [48], [54], but is limited in its restricted topological options. A memory-efficient implicit representation of the foams was also presented recently [55].

Designing an open-cell foam for free-form shapes has also been widely studied. They were mostly achieved by aligning with a pre-optimized density, stress, or material fields [7], [8], [11], [56], [57]. Most of them focused on 2D or 2.5D case [8], [56], [57]. An efficient 3D procedural modeling process was

introduced for open-cell foam construction with smoothly graded properties [7], [11]. A variational optimization will improve the convergence and the resulted foam performance. Lu et al. [14] achieved this with maximal cell hollowing and minimum stress by an adaptive Monte Carlo optimization approach. Its huge computational costs and closed cells limit industrial applications. Very recently, Feng et al. [15] proposed an attractive concept of differentiable Voronoi diagrams via a continuous distance field approximation. The approach demonstrated its high efficiency and nice ability in anisotropy and locality control. It however only produced *close-cell* foams in 3D. Differently, the proposed approach focuses on *open-cell* foams. In addition, it for the first time allows automatic tuning of the seed number and makes technical contributions to analyzing the foam’s differentiability with respect to the seeds, a very efficient local gradient approximation, and a much-accelerated simulation compared with direct FEM.

III. IDEA AND OVERVIEW

We begin our exposition with the basic idea of the explicit topology optimization for the design of Voronoi foams.

For explicit shape control, we use the edges of the Voronoi diagram with certain radii to form a Voronoi foam. The Voronoi seeds and the radii are called *geometry-based design variables*. The representation allows for intricate structure control with full connection even at extremely low volume fractions, compared with the voxel-based or lattice-based representation. Confining the Voronoi foam within a free-form outer shell naturally leaves out a shape-adapting foam.

Under such Voronoi tessellations for open-cell foam design, the topology optimization is to optimize the foam’s stiffness along with volume constraints and shape regularization requirements w.r.t the geometry-based design variables, that is, the seed positions and the beam radii. To reliably and efficiently solve the above problem, one must carefully address the following technical challenges:

- How to simulate the mechanical behavior of a Voronoi foam composed of many slender beams accurately.
- How to compute the derivatives about the edges (i.e. beams) in the Voronoi diagram w.r.t the design variables efficiently.
- How to efficiently adapt the key parameters like cell number and foam topology under various constraints reliably.

Three technical points are proposed for the challenges: a synchronized explicit and implicit form for modeling a Voronoi foam, a numerical coarsening approach for its simulation, and an efficient local finite difference approach to compute the gradients to guide the optimization. We coin the framework as the concept of *explicit topology optimization*.

Based on the above idea, the problem of explicit topology optimization of a Voronoi foam is formulated as a variational optimization problem. It is solved following the classical topology optimization framework and proceeds as Algorithm 1, as also illustrated in Fig. 1. The algorithm first embeds the domain with a coarse background mesh for downstream simulations (Step 1), and initializes the design

variables of seeds \mathbf{X} and radii \mathbf{r} (Step 2). The variable values are repeatedly updated until convergence following the consequent steps: density function computation (Step 4), property simulation (Step 5), gradient computation (Step 6), and design update (Step 7). Finally, the optimized Voronoi foam is constructed from \mathbf{X} , \mathbf{r} , Ω and output (Step 9). More technical details are explained below.

In step 4, we construct an implicit function to represent the Voronoi foam structure and produce a smooth foam under explicit geometry-based control variables. The implicit representation avoids the unreliable and very time-consuming geometry operations in explicitly constructing the Voronoi foams and generating simulation mesh, and allows for continuous FEM integration of high accuracy.

In step 5, a novel numerical coarsening for foam simulation is proposed. It conducts the simulation on the embedding coarse mesh constructed in Step 1, and still achieves high simulation accuracy by tailoring a set of polyhedral material-aware shape functions for each coarse element. The process works directly on the implicit foam representation, avoids error-prone boundary conforming fine mesh generation, and greatly reduces the computational costs.

In Step 6, we adopt finite difference and customize a three-point-based distance approximation approach to accelerate the gradient computation, utilizing the locality property of the Voronoi tessellations. It consequently alleviates the overall computational efforts by several orders of magnitude. Based on the gradient information, the foam is updated using the method of GCMMA (Generalized Convex Method of Moving Asymptotes) [58].

Algorithm 1 Explicit topology optimization of a Voronoi foam

Input: Design domain Ω , initial seed locations \mathbf{X} and radii \mathbf{r} , target volume fraction v , a weight ω that balance the foam's compliance and regularity.

Output: The optimized Voronoi foam of optimized compliance (and regularity) under constraints of volume fraction.

- 1: **Construct** a background coarse mesh to embed domain Ω .
 - 2: **Initialize** values of the seeds \mathbf{X} and radii \mathbf{r} .
 - 3: **repeat**
 - 4: **Compute** for the current seeds and radii its density function that represents a smooth Voronoi foam (intersected with Ω of certain thickness).
 - 5: **Conduct** the simulation on the foam via a novel numerical coarsening approach.
 - 6: **Compute** the gradients of the compliance and constraints with respect to \mathbf{X} and \mathbf{r} via a local finite difference strategy.
 - 7: **Update** the seeds \mathbf{X} and radii \mathbf{r} via GCMMA based on the gradients.
 - 8: **until** reaching convergence.
 - 9: **Outputs:** seeds \mathbf{X} and radii \mathbf{r} and the associated Voronoi foam.
-

IV. MATHEMATICAL FORMULATION

A. Implicit modeling of Open-cell Voronoi foams

In this study, an open-cell Voronoi foam is defined as edges (of certain radii) of Voronoi cells, confined within the model's interior. Blending the implicit functions of all the beams introduced by the Voronoi edges, or together with the

outer shell, we have an implicit representation of the Voronoi foam defined as a density field. Details are explained below.

Each Voronoi foam $\Omega^V(\mathbf{X}, \mathbf{r})$ is composed of two parts: the inner part and the boundary part. For the inner part, we first compute the Voronoi diagram from the seeds $\mathbf{X} = \{\mathbf{X}_i, i = 1, \dots, N_s\}$ in a large enough bounding box, then clip all its edges using the outer free-form shape Ω . The j -th remaining edge is turned into a beam with the radius \bar{r}_j averaged from the neighboring seeds:

$$\bar{r}_j = \sum_{i \in \mathcal{X}_j} r_i / |\mathcal{X}_j|, \quad (1)$$

where \mathcal{X}_j is the set of neighboring seeds of edge j , $|\mathcal{X}_j|$ is the number of seeds. The radii on seeds are collected in a vector \mathbf{r} . The image in Fig. 2(a) indicates the situation.

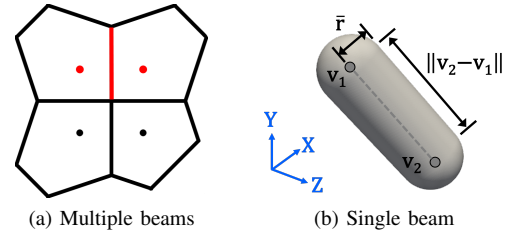


Fig. 2. The definition of beams: (a) A beam radius is defined from its adjacent seeds; (b) A single beam description.

Corresponding to a Voronoi edge of vertices $\mathbf{v}_1, \mathbf{v}_2$, a beam ϕ is defined which consists of a cylinder with radius \bar{r} and height $\|\mathbf{v}_2 - \mathbf{v}_1\|$ and two half-sphere ends with radius \bar{r} ; see Fig. 2. The implicit form $\tilde{\phi}$ of the beam ϕ is defined as follows,

$$\tilde{\phi}(\mathbf{x}) = \tilde{\phi}(\mathbf{x}, \mathbf{v}_1, \mathbf{v}_2, \bar{r}) = \bar{r} - d(\mathbf{x}, \mathbf{v}_1, \mathbf{v}_2), \quad (2)$$

where $d(\mathbf{x}, \mathbf{v}_1, \mathbf{v}_2)$ represents the minimum distance from the point \mathbf{x} to the edge $\mathbf{v}_1, \mathbf{v}_2$,

$$d(\mathbf{x}, \mathbf{v}_1, \mathbf{v}_2) = \begin{cases} \|\mathbf{b}\|, & \text{if } \mathbf{a} \cdot \mathbf{b} \leq 0, \\ \|\mathbf{g}\|, & \text{if } 0 < \mathbf{a} \cdot \mathbf{b} < \mathbf{a} \cdot \mathbf{a}, \\ \|\mathbf{e}\|, & \text{if } \mathbf{a} \cdot \mathbf{b} \geq \mathbf{a} \cdot \mathbf{a}, \end{cases} \quad (3)$$

for

$$\mathbf{a} = \mathbf{v}_2 - \mathbf{v}_1, \quad \mathbf{b} = \mathbf{x} - \mathbf{v}_1, \quad \mathbf{e} = \mathbf{x} - \mathbf{v}_2, \quad \mathbf{g} = \left(\mathbf{I} - \frac{1}{\|\mathbf{a}\|^2} \mathbf{a} \otimes \mathbf{a} \right) \mathbf{b}. \quad (4)$$

The implicit representation of the whole open-cell Voronoi foam is the union of the implicit functions of all beams after smoothing using Kreisselmeier-Steinhaus (KS) function [33],

$$\Phi(\mathbf{x}) = \frac{1}{p} \ln \left(\sum_{j=1}^n e^{p \cdot (\phi_j(\mathbf{x}) - \phi_{\max})} \right) + \phi_{\max}, \quad (5)$$

where $\phi_{\max} = \max(\phi_1, \dots, \phi_n)$ for the beam number n , and $p = 16$ in this paper. KS function makes the description function $\Phi(\mathbf{x})$ compact and differentiable w.r.t. \mathbf{x} . The different structures constructed using the union function and the KS function are compared in Fig. 3.

The boundary part related to the outer shape Ω is also represented in an implicit form $\phi_\Omega(\mathbf{x})$. When a closed shell is required, Eq. (5) is directly extensible by taking $\phi_\Omega(\mathbf{x})$ as

an additional beam. Otherwise, we include the intersections between the outer shapes and the Voronoi faces, where each face thickness is the average of the radii of the two seeds that determine the face. For simplicity, we will not distinguish the Voronoi foams with or without a shell.

The *Voronoi foam* $\Omega^V(\mathbf{X}, \mathbf{r})$ is ultimately described as a density field by a regularization Heaviside function $H(\Phi(\mathbf{x}))$,

$$H(\Phi(\mathbf{x})) = \begin{cases} 1, & \text{if } \Phi(\mathbf{x}) > \epsilon, \\ \frac{3(1-\alpha)}{4} \left(\frac{\Phi}{\epsilon} - \frac{\Phi^3}{3\epsilon^3} \right) + \frac{(1+\alpha)}{2}, & \text{if } -\epsilon \leq \Phi(\mathbf{x}) \leq \epsilon, \\ \alpha, & \text{otherwise,} \end{cases} \quad (6)$$

where ϵ controls the magnitude of regularization, $\alpha = 1e^{-6}$ by default is a small positive number to avoid a singular global stiffness matrix [59].

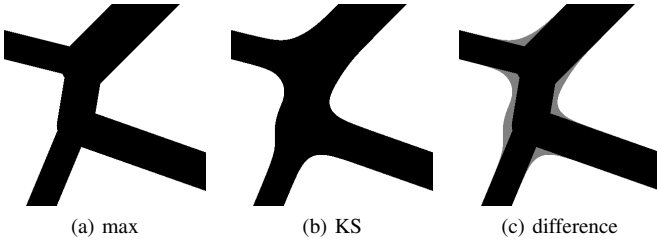


Fig. 3. Comparison between direct boolean and implicit beam blending.

The Voronoi foam design problem takes seeds and radii \mathbf{X}, \mathbf{r} as design variables for performance optimization. Its analytical and discrete formulations are explained below. We focus on the most popular problem of stiffness optimization [5].

B. Problem formulation as an optimization problem

Given seeds \mathbf{X} and radii \mathbf{r} , the material volume $V(\mathbf{X}, \mathbf{r})$ of the Voronoi foam is

$$V(\mathbf{X}, \mathbf{r}) = \int_{\Omega} H(\Phi(\mathbf{x})) dV. \quad (7)$$

The admissible space that constrains the volume of the Voronoi foam, denoted A , is defined as

$$A = \{(\mathbf{X}, \mathbf{r}) \mid V(\mathbf{X}, \mathbf{r})/V_0 \leq v, \underline{\mathbf{X}} \leq \mathbf{X} \leq \overline{\mathbf{X}}, \underline{\mathbf{r}} \leq \mathbf{r} \leq \overline{\mathbf{r}}\}, \quad (8)$$

where V_0 is the volume of design domain and v is a prescribed volume fraction. The lower and upper bounds of \mathbf{X} , i.e. $\underline{\mathbf{X}}, \overline{\mathbf{X}}$, are set according to the axis-aligned bounding box of Ω or from user prescription. The bounds of \mathbf{r} , for simulation accuracy, are set so that the width of a beam at least spans two fine mesh elements, i.e.

$$\underline{\mathbf{r}} \geq 2 l_a, \quad (9)$$

where l_a is the average edge length of fine mesh.

It should be noticed that for a model, seed number and beam radii determine a lower bound of the volume fraction if all the seeds are inside the model. Therefore, improper values of these parameters will bring infeasible settings. Fortunately, our method may move seeds out of the model and greatly alleviate the difficulty of setting parameters.

The domain containing the Voronoi foam is equipped with a non-uniform material by mapping the density $H(\Phi(\mathbf{x}))$ to the fourth-order elastic tensor $\mathbf{D}(\mathbf{x})$:

$$\mathbf{D}(\mathbf{x}, \mathbf{X}, \mathbf{r}) = H(\Phi(\mathbf{x})) \mathbf{D}_0, \quad (10)$$

where \mathbf{D}_0 is the constant elastic tensor in the solid regions. $\mathbf{D}(\mathbf{x})$ is correspondingly nearly zero in the void regions not covered by the beams.

Then, for a user-specified load $\boldsymbol{\tau}$, its associated static displacement \mathbf{u} under the test function \mathbf{v} in Sobolev vector space $H_0^1(\Omega)$ is characterized by an equation involving the strain vectors $[L\mathbf{u}], [L\mathbf{v}]$:

$$a(\mathbf{u}, \mathbf{v}, \mathbf{D}) = l(\mathbf{v}), \quad \forall \mathbf{v} \in H_0^1(\Omega), \quad (11)$$

where

$$a(\mathbf{u}, \mathbf{v}, \mathbf{D}) = \int_{\Omega} [L\mathbf{u}]^T \mathbf{D}(\mathbf{x}, \mathbf{X}, \mathbf{r}) [L\mathbf{v}] dV, \quad (12)$$

and

$$l(\mathbf{v}) = \int_{\Gamma_N} \boldsymbol{\tau} \cdot \mathbf{v} dS. \quad (13)$$

As the goal, we hope the overall deformation of the Voronoi foam $\Omega^V(\mathbf{X}, \mathbf{r})$ is small while simultaneously maintaining certain shape regularity. Therefore, we introduce two terms about compliance and shape. The compliance $C(\mathbf{X}, \mathbf{r}, \mathbf{u})$ measuring the elastic potential of the body, as widely adopted in topology optimization, is set as the physical objective,

$$C(\mathbf{X}, \mathbf{r}, \mathbf{u}) = \frac{1}{2} \int_{\Omega} [L\mathbf{u}]^T \mathbf{D}(\mathbf{x}, \mathbf{X}, \mathbf{r}) [L\mathbf{u}] dV. \quad (14)$$

The shape regulation energy $S(\mathbf{X})$ is to regularize the Voronoi cells to approximate regular polyhedrons

$$S(\mathbf{X}) = \sum_{i=1}^{N_s} w_{\mathbf{X}_i} \|\mathbf{X}_i - \mathbf{X}_i^c\|^2, \quad (15)$$

that is, the sum of the Euclidean distances between seed \mathbf{X}_i and the centroid \mathbf{X}_i^c of each Voronoi cell \mathcal{V}_i weighted by $w_{\mathbf{X}_i}$ [60]. $w_{\mathbf{X}_i} = 1$ is simply adopted here.

Finally, we get the constrained optimization problem:

$$\begin{aligned} \min_{(\mathbf{X}, \mathbf{r}) \in A, \mathbf{u}} \quad & J(\mathbf{X}, \mathbf{r}, \mathbf{u}) \\ \text{s.t.} \quad & a(\mathbf{u}, \mathbf{v}, \mathbf{D}) = l(\mathbf{v}), \quad \forall \mathbf{v} \in H_0^1(\Omega), \end{aligned} \quad (16)$$

where the design target $J(\mathbf{X}, \mathbf{r}, \mathbf{u})$ is set as the weighted sum of the physical objective and the shape regularization term,

$$J(\mathbf{X}, \mathbf{r}, \mathbf{u}) = (1 - w) C(\mathbf{X}, \mathbf{r}, \mathbf{u}) + w S(\mathbf{X}). \quad (17)$$

Notice here that different measures of physical performances or shape regularizations can be introduced for different design purposes, and the target foams can be derived similarly following the procedure described below.

C. Discretization

To discretize the displacement, strain, or stress fields, one can of course directly tessellate the foam by a boundary conforming fine mesh. However, we build a fixed background (linear tetrahedral) mesh $D = \{D_e, e = 1, 2, \dots, N\}$ to cover the shape Ω , i.e. $\Omega \subset D$. This choice brings two merits: avoiding the very time-consuming and error-prone generation of boundary conforming meshes and ensuring convergence of optimization by simulation on a fixed mesh.

In each tetrahedral element D_e , the density H_e is set to the average of $H(\mathbf{x})$ on its four nodes,

$$H_e(\mathbf{X}, \mathbf{r}) = \sum_{k=1}^4 H(\Phi(\mathbf{v}_e^k, \mathbf{X}, \mathbf{r}))/4, \quad (18)$$

for \mathbf{v}_e^k being the coordinate of k -th node in element D_e .

Giving the vector of discrete displacements \mathbf{Q} on the nodes of background mesh D , we collect the displacements on the nodes of e -th element D_e as \mathbf{Q}_e , then the displacement on any point of $\mathbf{x} \in D_e$ can be interpolated as

$$\mathbf{u}(\mathbf{x}) = \mathbf{N}_e(\mathbf{x})\mathbf{Q}_e, \quad (19)$$

where $\mathbf{N}_e(\mathbf{x})$ denotes the element linear bases (shape functions) on the nodes of e -th element. The element stiffness matrix \mathbf{K}_e can be further derived following a classical Galerkin FE method,

$$\mathbf{K}_e(\mathbf{X}, \mathbf{r}) = H_e(\mathbf{X}, \mathbf{r}) \int_{D_e} [\mathbf{LN}]^T \mathbf{D}_0 [\mathbf{LN}] dV. \quad (20)$$

The global stiffness matrix $\mathbf{K}(\mathbf{X}, \mathbf{r})$ can be simply assembled by summing $\mathbf{K}_e(\mathbf{X}, \mathbf{r})$. Now, the equilibrium equation Eq. (11) is discretized into the following equation

$$\mathbf{K}(\mathbf{X}, \mathbf{r})\mathbf{Q} = \mathbf{f}, \quad (21)$$

where \mathbf{f} is discretized load $\boldsymbol{\tau}$. Solving above equation to get the displacement vector \mathbf{Q} , the compliance C is computed from

$$C(\mathbf{X}, \mathbf{r}, \mathbf{u}) \approx \frac{1}{2} \|\mathbf{Q}\|_{\mathbf{K}(\mathbf{X}, \mathbf{r})}^2 = C(\mathbf{X}, \mathbf{r}, \mathbf{Q}). \quad (22)$$

V. GRADIENT-BASED OPTIMIZATION

After discretizing Eq. (16), we get the optimization problem:

$$\begin{aligned} \min_{(\mathbf{X}, \mathbf{r}) \in A, \mathbf{Q}} & (1-w)C(\mathbf{X}, \mathbf{r}, \mathbf{Q}) + wS(\mathbf{X}) \\ \text{s.t.} & \mathbf{K}(\mathbf{X}, \mathbf{r})\mathbf{Q} = \mathbf{f}. \end{aligned} \quad (23)$$

To eliminate the equilibrium state constraint, we treat \mathbf{Q} as the function of (\mathbf{X}, \mathbf{r}) via $\mathbf{Q}(\mathbf{X}, \mathbf{r}) = \mathbf{K}^{-1}(\mathbf{X}, \mathbf{r})\mathbf{f}$, and view C as function of (\mathbf{X}, \mathbf{r}) , i.e. $C(\mathbf{X}, \mathbf{r}) \triangleq C(\mathbf{X}, \mathbf{r}, \mathbf{Q}(\mathbf{X}, \mathbf{r}))$. Now, the above problem is turned into

$$\min_{(\mathbf{X}, \mathbf{r}) \in A} (1-w)C(\mathbf{X}, \mathbf{r}) + wS(\mathbf{X}). \quad (24)$$

A. Optimization solutions

Eq. (24) is to be solved following a numerical gradient-based approach. Both the topology and geometry of the Voronoi foams $\Omega^V(\mathbf{X}, \mathbf{r})$ are optimized simultaneously in this study. The GCMMA optimizer [58] is carefully chosen. It approximates the original nonconvex problem through a set of convex sub-problems by using the gradients of the optimization objective and constraints with respect to the design variables \mathbf{X} and \mathbf{r} derived below.

According to the chain rule and an adjoint approach [61], the sensitivity of the objective function $C(\mathbf{X}, \mathbf{r})$ is derived as follows:

$$\frac{\partial C(\mathbf{X}, \mathbf{r})}{\partial a} = -\frac{1}{2} \mathbf{Q}^T \frac{\partial \mathbf{K}}{\partial a} \mathbf{Q} = -\frac{1}{2} \mathbf{Q}^T \sum_e \frac{\partial \mathbf{K}_e}{\partial a} \mathbf{Q}. \quad (25)$$

According to Eq. (20), we have

$$\frac{\partial \mathbf{K}_e(\mathbf{X}, \mathbf{r})}{\partial a} = \frac{\partial H_e(\mathbf{X}, \mathbf{r})}{\partial a} \int_{D_e} [\mathbf{LN}]^T \mathbf{D}_0 [\mathbf{LN}] dV, \quad (26)$$

and

$$\frac{\partial H_e(\mathbf{X}, \mathbf{r})}{\partial a} = \frac{1}{4} \sum_{k=1}^4 \frac{\partial H(\Phi(\mathbf{v}_e^k, \mathbf{X}, \mathbf{r}))}{\partial a}, \quad (27)$$

where a denotes a component of the variables \mathbf{X}_i or \mathbf{r}_i .

One can easily identify two obvious challenges in the above procedure: First, the derivatives $\partial H/\partial a$ (in Eq. (27)) are related to the Voronoi diagram, whose differentiability is not clear and a direct finite-difference based computation is extremely expensive. Second, the complex geometry of the foam structure entails fully resolved finite element mesh, bringing about a huge number of DOFs in \mathbf{Q} and the prohibitive cost of solving the large linear system for \mathbf{Q} (in Eq. (25)).

The second issue is to be addressed in Section VI. The first issue is addressed below, where we explore its differentiability and develop an efficient numerical computation approach by exploiting the local property of the Voronoi diagram.

B. Differentiability analysis of Voronoi edge w.r.t to seeds

For a given parameter a as a component of \mathbf{X}, \mathbf{r} , the derivative $\partial H/\partial a$ boils down to terms about $\partial H/\partial \Phi$, $\partial \Phi/\partial \phi_j$ and $\partial \phi_j/\partial a$ via the chain rule from the implicit expression of H in Eq. (6). However, it is not always valid as it implicitly assumes the topology of the underlying Voronoi diagram remains unchanged within a small variation of seed points, which is however not always true. The minimal distance $\phi_j(\mathbf{x}_0, \mathbf{X}, \mathbf{r})$ is continuous but not always differentiable about a seed point \mathbf{X}_i at a specific vertex point $\mathbf{x} = \mathbf{x}_0$. Consider the example in Fig. 4, where we plot the curve $\phi(\mathbf{x}_0, \mathbf{X}, \mathbf{r})$, a distance function from a point \mathbf{x}_0 (in green) to the Voronoi foam $\Omega^V(\mathbf{X}, \mathbf{r})$, w.r.t. a seed \mathbf{X}_i . The distance function is always continuous. We notice the curve has some critical situations: when four seed points (three in black and one in red) share a circumscribed circle, the beam (in blue) that \mathbf{x}_0 is closest to is jumping from one to another.

The distance function $\phi(\mathbf{x}_0, \mathbf{X}, \mathbf{r})$ is however not always differentiable with respect to seeds \mathbf{X} in two situations: the above critical situation, and when \mathbf{x}_0 is on the Voronoi edge.

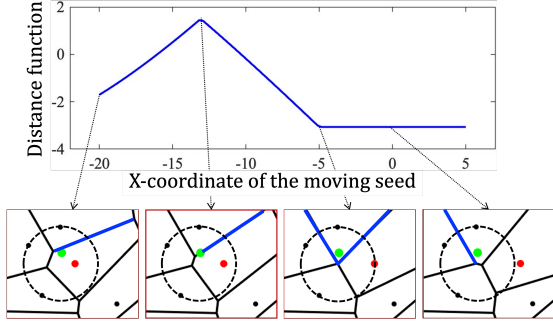


Fig. 4. The distance curve from a watching point (in green) to a Voronoi foam. The third figure below shows a critical situation in which four seeds (three in black and one in red) share a circumscribed circle. The beam that \mathbf{x}_0 is closest to is in blue.

Luckily, the number of such singular points is small and can be easily smoothed out [33]. The result is concluded below.

The distance function $\phi(\mathbf{x}_0, \mathbf{X}, \mathbf{r})$ is continuous but not always differentiable w.r.t seed points \mathbf{X}_i at finite number of points: 1. $\phi(\mathbf{x}_0, \mathbf{X}, \mathbf{r})$ takes its value at a critical point of $\Omega^V(\mathbf{X}, \mathbf{r})$ where four or more seed points share a common circumscribed circle/sphere. 2. \mathbf{x}_0 is on the Voronoi edge.

C. Numerics in derivative computations

The required derivatives Eq. (27) in solving problem Eq. (16) build up a Jacobian matrix of huge size $n \times 4N_s$, where n is the vertex number of background mesh D and $4N_s$ is the number of design variables. The number can reach as high as 1 billion ($1M \times 10K$) for the cube example in Fig. 18. It requires great computational effort even though the matrix is sparse. Further noticing that the distance function consists of a large number of beams, a direct computation for each derivative, either analytically or via finite difference, would be even prohibitive.

The efficiency is to be greatly improved here by exploring the locality of the Voronoi diagram. Firstly, the 2-ring criteria of Voronoi diagram tells that only seed points in a 2-ring around \mathbf{x}_0 influence the density on \mathbf{x}_0 [7]. Accordingly, we can generate the Voronoi diagram locally by carefully picking up these local seeds. It also much reduces the number of beams $\phi_j(\mathbf{x})$ to be used in the overall distance function computation in Eq. (6).

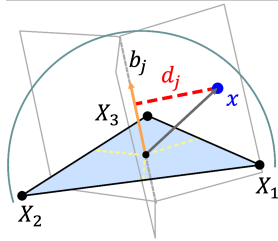


Fig. 5. Three-point distance approximation without explicit Voronoi tessellation. The signed distance is approximated as $\bar{r}_j - d_j$ for the beam radius \bar{r}_j .

We further develop a three-point distance approximation approach to improve the distance computation efficiency by

only considering the three nearest points to a given vertex \mathbf{x}_0 . It is assumed that the beam radii are approximately the same. Accordingly, as indicated in Fig. 5, let b_j be the beam determined by the three seeds $\mathbf{X}_1, \mathbf{X}_2, \mathbf{X}_3$, and d_j the distance from \mathbf{x}_0 to b_j . We set the value of the distance field at \mathbf{x}_0 approximately as $\bar{r}_j - d_j$ where \bar{r}_j is the averaged radii to the three points.

It can be roughly estimated that the approximated minimal distance has a maximal error $|r_2 - r_1|$ to its true value where r_1, r_2 are the minimal distances of the vertex \mathbf{x}_0 to its Voronoi diagram and its Voronoi foam. Accordingly, the density at \mathbf{x}_0 will not change, or $\bar{\rho} = \rho$, when $r_2 \leq 2r_1$.

Algorithm 2 Derivative computation of density field function

Inputs: Voronoi foam $\Omega^V(\mathbf{X}, \mathbf{r})$, a tetrahedral vertex \mathbf{x}_0 ;

Outputs: Derivative of the distance function $H(\Phi(\mathbf{x}_0, \mathbf{X}, \mathbf{r}))$ in Eq. (6) w.r.t. a seed \mathbf{X}_i ;

(1) Select the k -nearest seeds around \mathbf{x}_0 and the associated distance functions that may influence the density value at point \mathbf{x}_0 based on the 2-ring criteria. Collect the influencing distance functions as $\phi_j(\mathbf{x}, \mathbf{X}, \mathbf{r})$, $j \in J$.

(2) Compute the derivative of $\phi_j(\mathbf{x}_0, \mathbf{X}, \mathbf{r})$, $j \in J$ w.r.t. \mathbf{X}_i via finite difference by updating the density for a seed point variation as follows:

- Let $r_1 = \min(\{r_k\})$ and $r_2 = \max(\{r_k\})$. If $r_2 \leq 2r_1$, update the density at point \mathbf{x}_0 via three-point approximate approach;
 - Otherwise, update the density at point \mathbf{x}_0 via locally reconstructing the Voronoi foam for the k seeds.
-

VI. FOAM SIMULATION VIA NUMERICAL COARSENING

Simulating the Voronoi foam with high accuracy is very challenging because of its complex interior structure. There are many numerical coarsening methods, and one of the state-of-the-art methods [20], which shows advantages over previous approaches, is taken here. This method also takes the strategy of material aware bases [25].

A. Preliminaries

As in Section IV-C, the conventional FEM evaluates the element stiffness matrix \mathbf{K}_e on fine tetrahedral elements and assembles them into the global stiffness matrix \mathbf{K} . However, in the numerical coarsening method proposed in this section, we use the counterparts \mathbf{K}^α on coarse elements instead of \mathbf{K}_e to constitute \mathbf{K} .

Two kinds of meshes are involved here: (1) the coarse polyhedral mesh $D^H = \{D^\alpha, \alpha = 1, 2, \dots, M\}$, (2) the refined tetrahedral mesh $D^\alpha = \{D_e^\alpha, e = 1, 2, \dots, e^\alpha\}$ engulfed by each coarse polyhedral element. Figs. 6 and 7 present the coarse mesh D^H and fine mesh D^α for a 2D case. The number of fine elements $N = \sum_{\alpha=1}^M e^\alpha$ is much greater than that of coarse elements here, i.e. $M \ll N$. Two kinds of nodes are also involved, namely (1) nodes defined along boundaries of coarse elements, abbreviated as coarse nodes,

with their displacements \mathbf{Q}^H , (2) boundary nodes and interior nodes of fine tetrahedral mesh, with their displacements \mathbf{q}_b and \mathbf{q}_i , as indicated in Fig. 7.

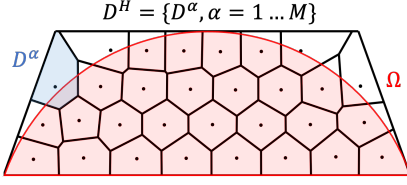


Fig. 6. Given a domain Ω , a background mesh D^H composed of coarse elements D^α is generated for numerical coarsening. D^H contains Ω .

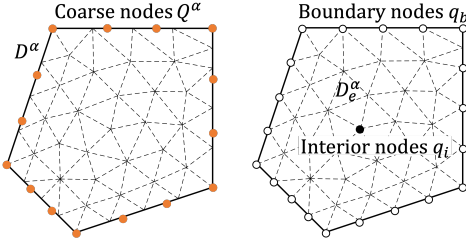


Fig. 7. Node definition. Boundary nodes and interior nodes are defined on the fine elements D_e^α , and coarse nodes are defined along the boundaries of the coarse element D^α . The coarse nodes do not have to be coincident with boundary nodes.

In our numerical coarsening method, coarse polyhedral mesh is used for simulation. For retaining sufficient accuracy, each coarse node is associated with a basis function (shape function) aware of the material inside, as indicated in Fig. 8. Significant efficiency improvement can be achieved owing to the smaller amount of DOFs.

Specifically, given the vector of discrete displacements \mathbf{Q}^H on coarse nodes, we collect the displacements on coarse nodes of α -th coarse element D^α as \mathbf{Q}^α . The displacements on a point $\mathbf{x} \in D^\alpha$ can be interpolated as

$$\mathbf{u}(\mathbf{x}) = \Phi^\alpha(\mathbf{x}) \mathbf{Q}^\alpha, \quad (28)$$

where $\Phi^\alpha(\mathbf{x})$ is the material-aware element basis function we use, defined on coarse nodes of D^α .

$\Phi^\alpha(\mathbf{x})$ is essentially a linear composition of linear bases on the fine mesh:

$$\Phi^\alpha(\mathbf{x}) = \mathbf{N}^\alpha(\mathbf{x}) \Psi^\alpha, \quad (29)$$

where $\mathbf{N}^\alpha(\mathbf{x})$ denotes the assembly of linear bases on the fine mesh of D^α , and Ψ^α is the transformation matrix from displacements \mathbf{Q}^α of coarse nodes to those \mathbf{q}^α of fine nodes,

$$\mathbf{q}^\alpha = \Psi^\alpha \mathbf{Q}^\alpha. \quad (30)$$

Substituting Eq. (29) and Eq. (30) into Eq. (28), we have

$$\mathbf{u}(\mathbf{x}) = \Phi^\alpha(\mathbf{x}) \mathbf{Q}^\alpha = \mathbf{N}^\alpha(\mathbf{x}) \mathbf{q}^\alpha, \quad (31)$$

i.e. the interpolated displacements are essentially obtained by linear shape functions on fine mesh.

Thus, the coarse element D^α stiffness matrix \mathbf{K}^α is given by Eq (20) using Φ^α instead of \mathbf{N}^α , i.e.

$$\begin{aligned} \mathbf{K}^\alpha(\mathbf{X}, \mathbf{r}) &= \int_{D^\alpha} [L\Phi^\alpha]^T \mathbf{D}(\mathbf{x}, \mathbf{X}, \mathbf{r}) [L\Phi^\alpha] dV \\ &= \sum_e^{e^\alpha} H_e(\mathbf{X}, \mathbf{r}) \int_{D_e^\alpha} (\Psi^\alpha)^T [LN^\alpha]^T \mathbf{D}_0 [LN^\alpha] \Psi^\alpha dV \\ &= (\Psi^\alpha)^T \left(\sum_e^{e^\alpha} H_e(\mathbf{X}, \mathbf{r}) \int_{D_e^\alpha} [LN^\alpha]^T \mathbf{D}_0 [LN^\alpha] dV \right) \Psi^\alpha \\ &= (\Psi^\alpha)^T \mathbf{k}^\alpha \Psi^\alpha, \end{aligned} \quad (32)$$

where \mathbf{k}^α is the high fidelity stiffness matrix for the fine mesh of D^α . In like wise, the gradient of the element stiffness matrix in Eq. (26) is computed in coarsened simulation as

$$\begin{aligned} \frac{\partial \mathbf{K}^\alpha(\mathbf{X}, \mathbf{r})}{\partial a} &= (\Psi^\alpha)^T \left(\sum_e^{e^\alpha} \frac{\partial H_e(\mathbf{X}, \mathbf{r})}{\partial a} \int_{D_e^\alpha} [LN^\alpha]^T \mathbf{D}_0 [LN^\alpha] dV \right) \Psi^\alpha \\ &= (\Psi^\alpha)^T \frac{\partial \mathbf{k}^\alpha}{\partial a} \Psi^\alpha. \end{aligned} \quad (33)$$

B. Shape functions as node value mapping

The remaining critical issue is the construction of transformation matrix Ψ^α , which takes into account the material inside. The material distribution changes with (\mathbf{X}, \mathbf{r}) , so Φ^α (i.e. Ψ^α) needs to be updated accordingly. Unlike [25], the approach in [20] does not require solving global harmonics on the fine mesh, so it is much faster and adopted here. However, the voxel coarse mesh with curved bridge nodes (CBNs) as coarse nodes is adopted in [20] for regular shapes, which cannot tightly approximate the free-form domain. For higher simulation accuracy, we extend the approach to handle more general coarse elements (e.g. tetrahedrons, or more versatile polyhedrons).

In our approach, Ψ^α in Eq. (29) is derived as a product of *boundary–interior transformation matrix* \mathbf{M}^α and *boundary interpolation matrix* ψ^α , as,

$$\Psi^\alpha = \mathbf{M}^\alpha \psi^\alpha, \quad (34)$$

where ψ^α and \mathbf{M}^α maps the displacements from the coarse nodes \mathbf{Q}^α to the boundary nodes \mathbf{q}_b and then to the full fine nodes \mathbf{q}^α . The construction of the two transformation matrices is explained below.

C. Boundary–interior transformation matrix

Firstly, \mathbf{M}^α is derived from the local FE analysis on the fine mesh of D^α just following procedures in Section IV-C, with the equilibrium equation

$$\begin{bmatrix} \mathbf{k}_b & \mathbf{k}_{bi} \\ \mathbf{k}_{ib} & \mathbf{k}_i \end{bmatrix} \begin{bmatrix} \mathbf{q}_b \\ \mathbf{q}_i \end{bmatrix} = \begin{bmatrix} \mathbf{f}_b \\ 0 \end{bmatrix}, \quad (35)$$

where $\mathbf{k}_b, \mathbf{k}_i, \mathbf{k}_{bi}, \mathbf{k}_{ib}$ are the sub-matrices of the fine tetrahedral mesh stiffness matrix \mathbf{k}^α , and \mathbf{f}_b the vector of exposed forces on the boundary nodes.

TABLE I
COMPARISONS BETWEEN OUR APPROACH AND OTHER ALTERNATIVES ON A 2D BRIDGE MODEL IN FIG 10 AND 3D FEMUR MODEL IN FIG. 11

	Infill	s-Infill	BTO	Lattice	Ours	Our Fixed-Seeds
Free topology variation	•	•	•	-	•	-
free-form adaption	•	•	-	-	•	•
Full connection	-	•	-	•	•	•
No gray element	-	-	-	•	•	•
Effective simulation	-	-	-	-	•	•
Compliance on 2D model (Fig. 10) ¹ ↓	409.8	401.8	1.3e ¹³	766.7	661.8	759.1
Compliance on 3D model (Fig. 11) ¹ ↓	125.1	137.1		104.8 ²	89.3	

¹ the ↓ indicates *the lower the better*. ² result from the *conforming* approach [31].

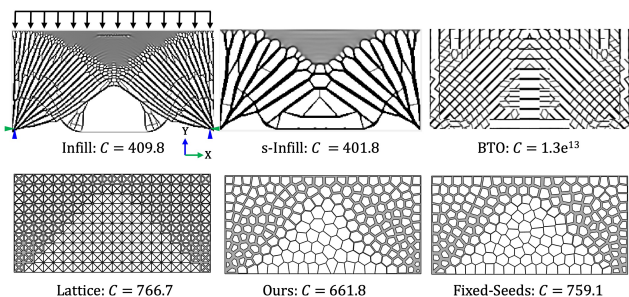


Fig. 10. Comparisons between different optimization approaches. Gray elements were observed for *Infill*, *s-Infill* and *BTO*, which may result in foams without full connectivity; Fixed topology was used for *Lattice* and *Fixed-Seeds*, which resulted in foams of worst properties. More comparisons are explained in Table I. Here, C is the compliance at convergence. Results from *Infill* and *s-Infill* were generated in 1,000 iterations.

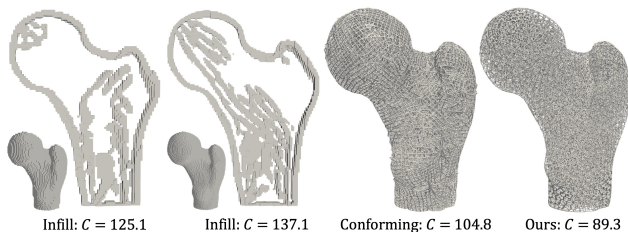


Fig. 11. Comparisons with related approaches *Infill* and *Conforming*. Undesired broken parts or protrusions were observed in sections of shapes obtained by *Infill* (the left two, respectively of 120,412 and 286,566 hexahedral elements). Ours produced a foam of valid geometry and best property (the rightmost); the middle right is the results produced by *Conforming* with higher compliance (worse performance).

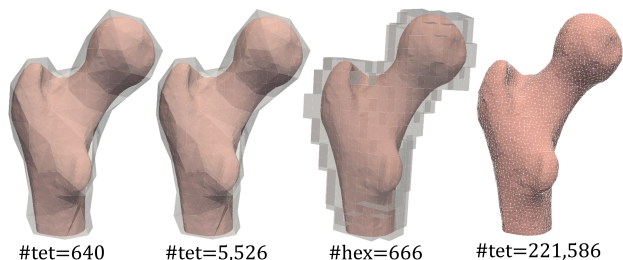


Fig. 12. Different FE meshes during optimization, from left to right: our coarse mesh, a tet-mesh 8x finer than the coarsest, a hex-mesh similar to the coarsest one, the finest one (as reference) similar to our fine mesh.

A. Explanations on other alternatives

We evaluate the approach’s performance by its comparisons with other alternatives via topology optimization, fixing cell

types, or different simulations. It includes:

- *Infill*: density-based topology optimization under constraints on local material volume in the proximity of each voxel [30]. Matlab code from <https://www.dropbox.com/s/77bhmh3lnf5qxdjs/Infill.m> was adopted.
- *s-Infill*: improved version for *infill*, where the initial density is set from the stress field derived from the full solid domain [34]. Matlab code from https://github.com/Junpeng-Wang-TUM/Infill_plus was adopted.
- *BTO*: density-based concurrent biscale topology optimization that simultaneously optimizes both the microstructures and their global distribution. Matlab code from [64] was adopted.
- *Lattice*: solely size optimization of a hierarchical lattice structure composed of the same type of substructures [42].
- *Conforming*: field-directed lattice optimization by aligning the beam directions along with optimized principal stress directions and the boundary of the optimized shape. Results from [31] were adopted.
- *Ours*: our parameter-based topology optimization of Voronoi foams by optimizing both the seeds’ locations and the beam radii; see Section VI.
- *Fixed-Seeds*: our approach but fixing the positions of seeds, i.e. only optimizing their radii.

We also make some comments. (1) Density-based approaches, such as *Infill*, *s-Infill*, *BTO*, generally have difficulty in shape control, and tend to produce gray elements or structures without full connection. Parameter-based approaches, such as *Lattice*, *Fixed-Seeds*, usually produce foams of fixed topology although our approach is an exception. (2) Simulation based on numerical homogenization, in comparison with the benchmark FEM, has much less simulation accuracy. In addition, it only works well for regular grids and is thus not applicable to the studied free-form foams. (3) Owing to its implicit representation, the proposed approach achieves smooth transitions among the bars or between the bars and the outer shell, which was seldom observed in previous studies; see also the close-up in Fig. 1. (4) Compared with a macro-structure generated from traditional topology optimization [65], whose compliance usually tends to be smaller (better), the foam has its own merits of damage tolerance, allowing the structure to maintain high stiffness even if some parts are broken, as well as robustness with respect to force variations [30].

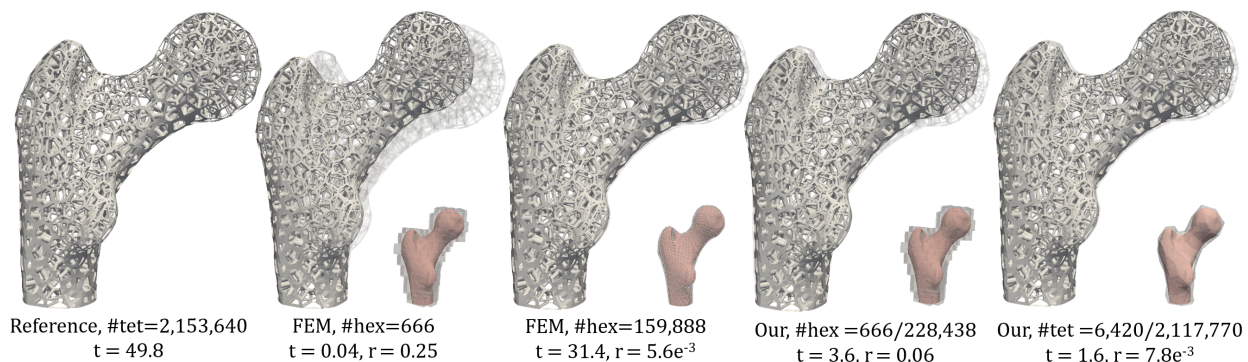


Fig. 13. Accuracy test: FEM comparison between fine tet-mesh (reference), background coarse hex-mesh, background fine hex-mesh, and ours on background coarse hex-mesh and ours on background coarse tet-mesh, from left to right. t is the time (seconds) of each simulation and r is the error defined in Eq. (42).

B. Comparisons with other alternatives

The results of comparisons are listed in Table I and detailed below. Amongst all the approaches, our approach is the unique that demonstrates the nice properties of free topology variations, free-form adaption, full connection, no gray elements, effective simulation, and low compliance (better properties).

2D Comparisons. Consider a 2D bridge problem in a regular domain in Fig. 10 of target volume fraction 0.4. Resolutions of the fine mesh and coarse mesh are 320×640 and 10×20 , and the number of seeds is 300. In the tests, *Infill* had convergence difficulty and generated large gray areas, due to its large number of local volume constraints [34]. Approach *s-Infill* improved the convergence rates and generated a reliable infill structure of the lowest compliance; it however induced unclear gray elements and did not produce foam-like structure. *BTO* produced an invalid foam mainly due to its low-accuracy numerical homogenization, where a huge difference between C and C_t was observed. Optimizations from *Lattice* or *Fixed-Seeds* generated geometrically valid foams but at a large performance reduction of increased compliance (worse stiffness). Our method generated a foam of valid geometry and smaller compliance. Moreover, our method ensures the full connection and structural smoothness of the resulted foam, as shown in Fig. 1, which are not available in density-based approaches.

3D Comparisons. Our approach was also tested for 3D models in comparison with two very related approaches *Infill* and *Conforming*. The femur model in [31] was used, slightly different from ours in Fig. 1. The target volume fraction was set to 0.5, and the results were plotted in Fig. 11.

To produce foams of similar beam numbers and beam sizes, the following settings were taken. Ours had 5,000 seeds, 2,001 coarse elements, and all together 697,570 fine tetrahedral elements; $w = 0.1$ in Eq. (17). *Infill* was conducted on two meshes respectively of 120,412 and 286,566 hexahedral elements. *Conforming* generated a foam of 59,423 beams (ours has 59,099 beams).

Both ours and *Conforming* generated structures of valid geometry while *Infill* produced some undesired broken parts or protrusions. In addition, ours gave the best foam with the smallest compliance, demonstrating its high effectiveness. The time costs per iteration of *Conforming*, *Infill* and ours are

respectively: 54.8s¹, 56.9s and 396.0s.

Comparisons with direct FEM. We tested the necessary of using the high-accuracy numerical coarsening during optimization by comparing the performance of the resulted foams obtained via FEM on four different background meshes shown in Fig. 12, using the femur model in Fig. 1. The finest is taken as a reference. Each coarse element’s Young’s modulus is averaged from those of its interior fine elements, following a common practice. Table II summarizes the results. Our method produced almost the same compliance as the reference, both of $C_t = 257.6$, and converged fastest in only 91 iterations and 1310.4 seconds, standing out as the most efficient. The other four mesh cases produced worse performance and were more difficult to converge.

TABLE II
THE OPTIMIZATION RESULTS USING FEM ON DIFFERENT MESHES FOR THE FEMUR MODEL IN FIG. 1.

Method	#ele	#iter ↓	C ↓	C_t ↓	total time
FEM _{tet}	640	- ¹	173.9	288.2	- ¹
FEM _{tet}	5,526	180	228.9	265.9	1854.0
FEM _{hex}	666	- ¹	162.4	298.6	- ¹
FEM _{tet}	221,586	110	257.6	257.6	5346.0
Ours	640	91	234.6	257.6	1310.4

¹ not converged at 200 iterations.
#ele, number of fine elements; #iter, iterations; C , compliance at convergence; C_t , true compliance computed via FEA; time (in seconds) of each iteration. The ↓ indicates *the lower the better*.

The simulation accuracy was also evaluated by comparing simulation results on the four different meshes, as plotted in Fig. 13. The approximation errors are $r = 0.25$, $r = 5.6e^{-3}$, $r = 0.06$, $r = 7.8e^{-3}$. Our CBN-based simulation showed a very close approximation to the reference. It also has a much-improved accuracy in comparison with other numerical homogenization approaches, as extensively studied in [20].

C. Timings and convergence.

Timings. The computation time is summarized in Table III. Overall, the simulation time depends on the fine mesh resolutions, and the optimization time additionally depends on the seed number. Benefiting from its local approximation,

¹data from [31] for a reference

TABLE III

TIMING (IN SECONDS) OF VORONOI TESSELLATIONS (PER-VOR), COMPUTATION OF SIGNED DISTANCE FUNCTIONS (PER-DIST), SIMULATION (PER-SIMU), FINITE DIFFERENCE (PER-DIFF) IN EACH ITERATION, AND OVERALL COST (PER-ITER) OF THE EXAMPLES ON INTEL 11700 CPU. SIZES OF GLOBAL FINE MESH, COARSE MESH, AND THE NUMBER OF SEEDS ARE ALSO SUMMARIZED.

Model	Fig. (L/M/R)	#fine	#coarse	#seed	time per-vor	time per-dist	time per-simu	time per-diff	time per-iter
femur	1	221,004	640	500	2.19	3.01	0.71	2.65	8.67
dome	20	206,825	122	122	0.33	0.20	8.49	1.79	10.99
shearing	18 (L)	260,608	512	1,000	1.10	2.17	3.14	3.26	9.79
insole	19 (L)	117,946	411	500	1.24	0.92	1.04	1.31	4.59

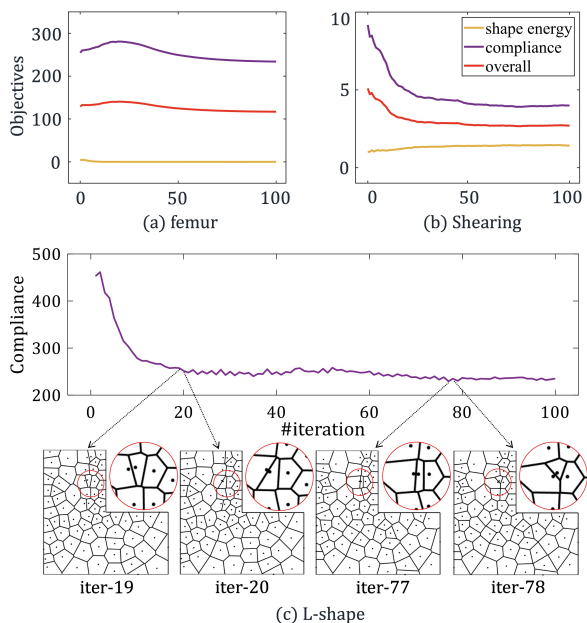


Fig. 14. Convergence curves of three test cases: (a) femur in Fig. 1, (b) shearing cube in Fig. 18, and (c) L-shape model with the Voronoi tessellations at some steps.

the gradients were efficiently achieved. A direct Voronoi tessellations based approach would be much more expensive, for example, 6,035 seconds for the femur model in Fig. 1.

Convergence. The convergence curves were plotted in Figs. 14(a)(b) for two typical tests: femur in Fig. 1 and shearing cube in Fig. 18. The two cases all showed global convergences. To watch closely, Fig. 14(c) plots the Voronoi variations for a concave 2D L-shape during optimization. Two pairs of exemplar cases were picked up: iter-19 to iter-20 with compliance increasing and iter-77 to iter-78 with compliance decreasing. Drastic cell topology variations were observed for both cases, which may cause inaccurate gradient computations (see also Sec. V-C) and consequently the unsmooth convergence. Still, an optimized Voronoi foam was robustly obtained.

D. Influence of parameter selections

Different initial seeds. We tested the method’s adaptivity to the numbers and positions of initial seeds using the femur model in Fig. 1 for four different seed sets: of random 500 seeds (500-1, 500-2) and 1000 seeds (1000-1, 1000-2). As shown in Fig. 15, very close compliance was observed

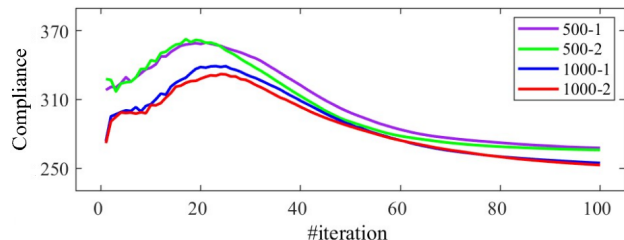


Fig. 15. Convergence curves under four different initial seeds, for the femur model in Fig. 1. Two (500-1, 500-2) contain 500 seeds with different positions, and another two (1000-1, 1000-2) contain 1000 seeds with different positions.

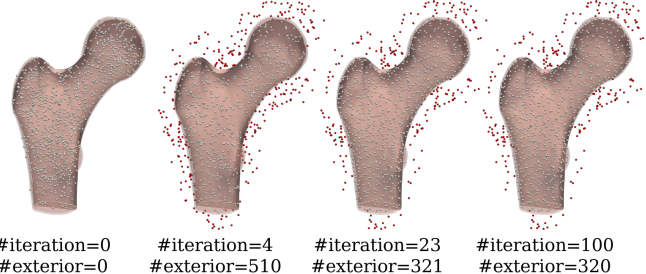


Fig. 16. Seed positions in four iterations for a case of 1000 seeds, where the white seeds are interior and the red are exterior. The exterior seeds did not contribute to the optimization model.

for cases of the same amount of seeds, illustrating the independence of initial seed positions. Slightly stiffer foams (with smaller compliance) were generated with 1000 seeds, of compliances 267.7 and 254.6 respectively for 500 and 1000 seeds.

The approach also demonstrated its capability to adjust the seed number by automatically moving unnecessary seeds outside of the outer shape. The seed movements were plotted in Fig. 16. Consider the 1000-1 case. 680 seeds out of 1000 contributed to the final Voronoi foam, with a volume fraction from 0.31 to 0.25. Benefiting from this, a rough estimate of the amount of seeds is sufficient for the users, avoiding multiple tedious attempts. We also conducted an optimization again using only the resulted 680 seeds inside the shape and removed all the outside ones. It finally produced an optimized foam of almost the same compliance but had only 538 seeds inside. It is not strange as there can be many solutions for a foam structure with many delicate micro entities if just a few requirements are posed (e.g. compliance). The experiment shows that our method can find various good solutions in a large design space. This ability implies the possibility of introducing more constraints and requirements of foam design.

Different finite difference steps. We tested the method’s convergence and stability for the femur model under different finite-difference steps: 0.5x, 1x, 2x, and 4x the average side length of fine elements. The convergence curves of the compliance C in Fig. 17 showed an overall convergence. The case of step=1x gave the stiffest foam and was set as default.

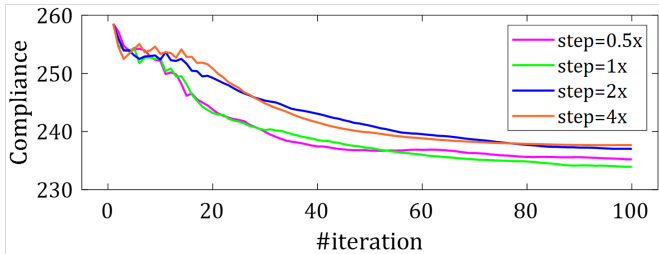


Fig. 17. Convergence curves of finite differences under four different steps, of 0.5, 1, 2, 4 times the average edge length of fine elements, for the femur model in Fig. 1.

E. Practical applications in different cases

Low volume fractions. We tested the approach’s capacity under extremely low volume fractions $v = 0.02, 0.05, 0.1$ using the shearing cube in Fig. 18. The case is very challenging for voxel-based topology optimization, where each foam cell needs approximately 100^3 voxels to capture the details. The overall foam needs around 1-billion voxels. It would be too computationally expensive, not to mention its difficulty in valid geometry control. Our approach only needs 4,000 design variables for the optimization.

Different loading forces. Results were shown in Fig. 19 on an insole model at three different loadings: real foot pressure, constant pressure, and constant pressure of 3x higher distribution in the heel or the front [66]. Denser seed distributions and larger radii appeared in the larger pressure area to maintain stronger stiffness.

Shape regularization weights. The shape regularization weight w in Eq. (16) was set of three different values $w = 0.1, 0.5, 0.9$, on a dome model of coarse polyhedral mesh in Fig. 20. The smaller w , the stiffer model with smaller compliance and worse shape regularization were generated. This is consistent with our heuristics. The dome model took more computation time, perhaps because of its denser stiffness matrix from its polyhedral background mesh.

Failure cases. Our approach may fail in some cases. First, it may produce large empty regions for shapes of sharp corners because of the boundary clipping. For example, in the right ear region in the Armadillo in Fig. 21, most region of the cusp was cut out, only leaving the intersected Voronoi edges. Introducing more Voronoi seeds around the region would help resolve the issue. Second, our numerical coarsening approach may not well simulate the model that has separate parts very close to each other. The parts may be embedded in the same coarse element and thus mistaken as mechanically attached. Considering separate yet superimposed embeddings for separate parts provides an option for addressing the issue [24]. These issues are to be explored in our future work.

VIII. CONCLUSION AND FUTURE WORK

We propose an explicit topology optimization method for open-cell foam design using Voronoi tessellation. Its usage of synchronized explicit and implicit representation in modeling, simulation, and optimization offers unique advantages in reliable and efficient Voronoi foam optimization. It also answers two general critical technical questions in implementing the goal of efficient gradient computation and reliable property simulation. As the extensive examples demonstrate, at very reasonable computational budgets, the approach is always able to produce a foam structure of full connectivity, extensive topology, and better properties, which were never observed in conventional voxel-based or lattice-based foam optimization approaches.

Practical fabricating the designed Voronoi foams may require additional supports [67]. On the other hand, the explicit geometric parameters of Voronoi foams, including seed locations and bar radii, are believed to be able to facilitate the inclusion of various manufacturing constraints into the foam optimization, such as bar length, cell size, relative bar-bar angles, and beam hanging angles, etc. In achieving the goal, relations between these manufacturing constraints with the design variables, in particular the seed locations, have to be derived. A recent work on differentiable surface triangulation [68] may provide insights into the study.

The approach opens a new avenue for reliable topology optimization of porous foams by maintaining full connectivity, resolving the open question in topology optimization [5]. Noticing that any 2D triangulation can be represented through a perturbation of a weighted Delaunay triangulation, a dual form of Voronoi tessellation [69]. The approach may thus be of great generality in producing general open-cell foams. The topic is to be explored in our future work. At present, it at least can be extended as follows. First, we are to devise fully analytical derivatives for a more stable and efficient of Voronoi foam optimization. Second, the open-cell foam has a distinguishing property of impact absorption than a close-cell one. Extending the approach for the associated topology optimization is to be studied, which must account for the non-linear large deformations. Third, we will explore approaches in introducing manufacturing constraints or/and anisotropy [70]–[72] into the Voronoi foam to improve its performance. In addition, it is also worthy of research efforts in optimizing restricted Voronoi foams [73] to produce a “conforming” foam where no cell clip is required and exploring its performance.

ACKNOWLEDGMENTS

We would like to thank all the anonymous reviewers for their valuable comments and suggestions. The work described in this paper is partially supported by the National Key Research and Development Program of China (No. 2020YFC2201303), the NSF of China (No. 62372401), the Key R&D Program of Zhejiang Province (No. 2022C01025), and the Zhejiang Provincial Science and Technology Program in China (No. 2021C01108).

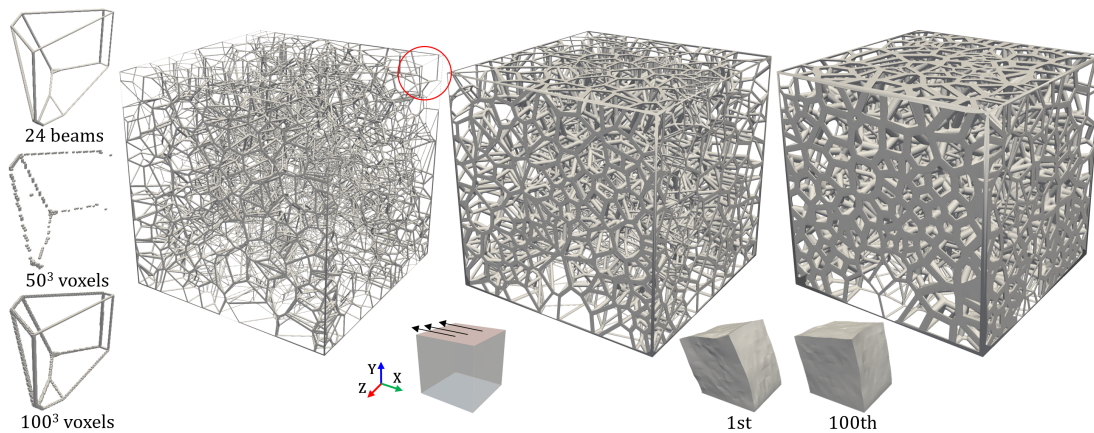


Fig. 18. Different volume fractions of extremely small values $v = 0.02, 0.05, 0.1$. Under the shearing boundary conditions, the deformations of the foams with $v = 0.02$ at 1st iteration and 100th iteration are plotted at the bottom, respectively of compliances 7.6 and 4.4. The left plots the voxel-based representations for a typical Voronoi cell at different resolutions.

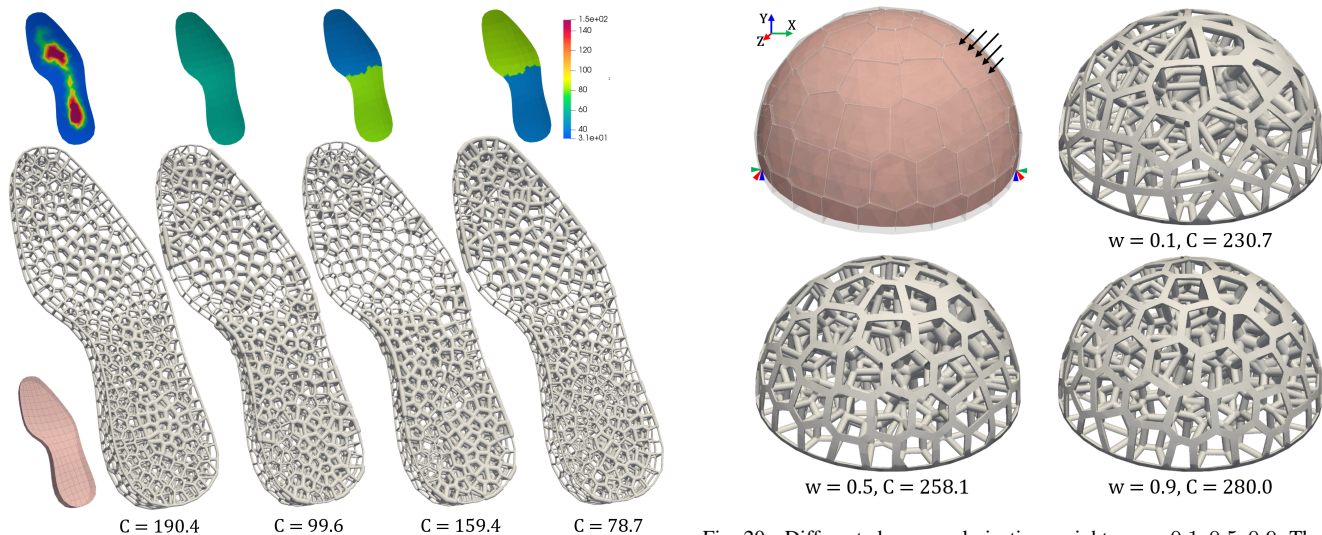


Fig. 19. Different loading forces, including mimicking real foot pressure, constant pressure, constant pressure of 3x higher distribution in the heel or the front. The compliances have been scaled $1e^{-6}$ times.

REFERENCES

- [1] C. Pan, Y. Han, and J. Lu, "Design and optimization of lattice structures: A review," *Applied Sciences*, vol. 10, no. 18, 2020.
- [2] M. C. Fernandes, J. Aizenberg, J. C. Weaver, and K. Bertoldi, "Mechanically robust lattices inspired by deep-sea glass sponges," *Nature Materials*, vol. 20, no. 2, pp. 237–241, 2021.
- [3] Y. Zhang, F. Zhang, Z. Yan, Q. Ma, X. Li, Y. Huang, and J. A. Rogers, "Printing, folding and assembly methods for forming 3D mesostructures in advanced materials," *Nature Reviews Materials*, vol. 2, no. 4, 2017.
- [4] S. H. Siddique, P. J. Hazell, H. Wang, J. P. Escobedo, and A. A. Ameri, "Lessons from nature: 3D printed bio-inspired porous structures for impact energy absorption – a review," *Additive Manufacturing*, vol. 58, p. 103051, 2022.
- [5] J. Wu, O. Sigmund, and J. P. Groen, "Topology optimization of multi-scale structures: a review," *Structural and Multidisciplinary Optimization*, vol. 63, no. 3, pp. 1455–1480, 2021.
- [6] Y. Liu, G. Zheng, N. Letov, and Y. F. Zhao, "A survey of modeling and optimization, methods for multi-scale heterogeneous lattice structures," *Journal of Mechanical Design, Transactions of the ASME*, vol. 143, no. 4, 2021.
- [7] J. Martínez, J. Dumas, and S. Lefebvre, "Procedural Voronoi foams for additive manufacturing," *ACM Transactions on Graphics*, vol. 35, no. 4, pp. 44:1–12, 2016.

Fig. 20. Different shape regularization weights $w = 0.1, 0.5, 0.9$. The main bearing beams with smaller w tend to be thicker than those with bigger w .

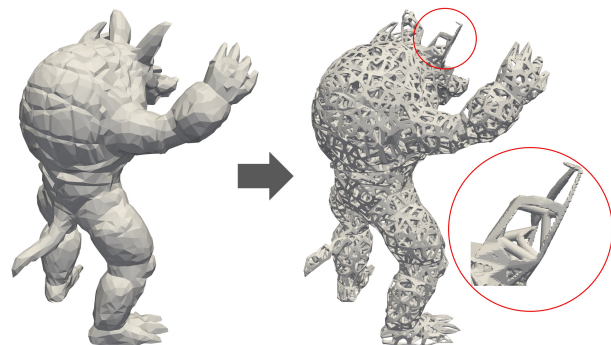


Fig. 21. Our approach may produce a foam of large empty regions around sharp corners.

- [8] Q. T. Do, C. H. P. Nguyen, and Y. Choi, "Homogenization-based optimum design of additively manufactured Voronoi cellular structures," *Additive manufacturing*, vol. 45, p. 102057, 2021.
- [9] L. J. Gibson and M. F. Ashby, *Cellular solids : structure and properties*. Cambridge University Press, 1997.

- [10] T. Stankovic and K. Shea, "Investigation of a Voronoi diagram representation for the computational design of additively manufactured discrete lattice structures," *Journal of Mechanical Design*, vol. 142, no. 11, pp. 1–21, 2020.
- [11] J. Martínez, H. Song, J. Dumas, and S. Lefebvre, "Orthotropic k-nearest foams for additive manufacturing," *ACM Transactions on Graphics*, vol. 36, no. 4, pp. 121:1–12, 2017.
- [12] J. Martínez, S. Hornus, H. Song, and S. Lefebvre, "Polyhedral Voronoi diagrams for additive manufacturing," *ACM Transactions on Graphics*, vol. 37, no. 4, pp. 129:1–15, 2018.
- [13] J. M. Podestá, C. G. Mendez, S. Toro, A. E. Huespe, and J. Oliver, "Material design of elastic structures using Voronoi cells," *International Journal for Numerical Methods in Engineering*, vol. 115, no. 3, pp. 269–292, 2018.
- [14] L. Lu, A. Sharf, H. Zhao, Y. Wei, Q. Fan, X. Chen, Y. Savoye, C. Tu, D. Cohen-Or, and B. Chen, "Build-to-last: Strength to weight 3D printed objects," *ACM Transactions on Graphics*, vol. 33, no. 4, pp. 1–10, 2014.
- [15] F. Feng, S. Xiong, Z. Liu, Z. Xian, Y. Zhou, H. Kobayashi, A. Kawamoto, T. Nomura, and B. Zhu, "Cellular topology optimization on differentiable Voronoi diagrams," *International Journal for Numerical Methods in Engineering*, vol. 124, no. 1, pp. 282–304, 2022.
- [16] G. Papanicolau, A. Bensoussan, and J.-L. Lions, *Asymptotic Analysis for Periodic Structures*. Elsevier, 1978, vol. 5.
- [17] O. Sigmund, "Materials with prescribed constitutive parameters: An inverse homogenization problem," *International Journal of Solids and Structures*, vol. 31, no. 17, pp. 2313 – 2329, 1994.
- [18] E. Andreassen and C. S. Andreasen, "How to determine composite material properties using numerical homogenization," *Computational Materials Science*, vol. 83, pp. 488–495, 2014.
- [19] D. A. White, J. Kudo, K. E. Swartz, D. A. Tortorelli, and S. E. Watts, "A reduced order model approach for finite element analysis of cellular structures," *Finite Elements in Analysis and Design*, vol. 214, p. 103855, 2023.
- [20] M. Li and J. Hu, "Analysis of heterogeneous structures of non-separated scales using curved bridge nodes," *Computer Methods in Applied Mechanics and Engineering*, vol. 392, p. 114582, 2022.
- [21] A. F. Bower, *Applied Mechanics of Solids*. CRC press, 2009.
- [22] L. Kharevych, P. Mullen, H. Owhadi, and M. Desbrun, "Numerical coarsening of inhomogeneous elastic materials," *ACM Transactions on Graphics*, vol. 28, no. 3, p. 51, 2009.
- [23] D. Chen, D. I. Levin, S. Sueda, and W. Matusik, "Data-driven finite elements for geometry and material design," *ACM Transactions on Graphics*, vol. 34, no. 4, pp. 1–10, 2015.
- [24] M. Nesme, P. G. Kry, L. Jeřábková, and F. Faure, "Preserving topology and elasticity for embedded deformable models," *ACM Transactions on Graphics*, vol. 28, no. 3, p. 52, 2009.
- [25] J. Chen, H. Bao, T. Wang, M. Desbrun, and J. Huang, "Numerical coarsening using discontinuous shape functions," *ACM Transactions on Graphics*, vol. 37, no. 4, pp. 1–12, 2018.
- [26] D. Schillinger and M. Ruess, "The finite cell method: A review in the context of higher-order structural analysis of CAD and image-based geometric models," *Archives of Computational Methods in Engineering*, vol. 22, no. 3, pp. 391–455, 2015.
- [27] C. Schumacher, B. Bickel, J. Rys, S. Marschner, C. Daraio, and M. Gross, "Microstructures to control elasticity in 3D printing," *ACM Transactions on Graphics*, vol. 34, no. 4, pp. 136:1–13, 2015.
- [28] B. Zhu, M. Skouras, D. Chen, and W. Matusik, "Two-scale topology optimization with microstructures," *ACM Transactions on Graphics*, vol. 36, no. 5, pp. 164:1–16, 2017.
- [29] H. Liu, Y. Hu, B. Zhu, W. Matusik, and E. Sifakis, "Narrow-band topology optimization on a sparsely populated grid," *ACM Transactions on Graphics*, vol. 37, no. 6, pp. 1–14, 2018.
- [30] J. Wu, N. Aage, R. Westermann, and O. Sigmund, "Infill optimization for additive manufacturing - approaching bone-like porous structures," *IEEE Transactions on Visualization and Computer Graphics*, vol. 24, no. 2, pp. 1127–1140, 2018.
- [31] J. Wu, W. Wang, and X. Gao, "Design and optimization of conforming lattice structures," *IEEE Transactions on Visualization and Computer Graphics*, vol. 27, no. 1, pp. 43–56, 2019.
- [32] E. Fernández, K.-k. Yang, S. Koppen, P. Alarcón, and S. Bauduin, "Imposing minimum and maximum member size, minimum cavity size, and minimum separation distance between solid members in topology optimization," *Computer Methods in Applied Mechanics and Engineering*, vol. 368, p. 113157, 2020.
- [33] W. Zhang, Y. Zhou, and J. Zhu, "A comprehensive study of feature definitions with solids and voids for topology optimization," *Computer Methods in Applied Mechanics and Engineering*, vol. 325, pp. 289–313, 2017.
- [34] J. Wang, J. Wu, and R. Westermann, "Stress topology analysis for porous infill optimization," *Structural and Multidisciplinary Optimization*, vol. 65, no. 3, pp. 1–13, 2022.
- [35] *Stress Trajectory Guided Structural Design and Topology Optimization*, ser. International Design Engineering Technical Conferences and Computers and Information in Engineering Conference, vol. Volume 2: 42nd Computers and Information in Engineering Conference (CIE), 08 2022.
- [36] J. Hu, S. Wang, Y. He, Z. Luo, N. Lei, and L. Liu, "A parametric design method for engraving patterns on thin shells," *IEEE Transactions on Visualization and Computer Graphics*, vol. 14, no. 18, pp. 1–12, 2023.
- [37] E. Garner, H. M. Kolken, C. C. Wang, A. A. Zadpoor, and J. Wu, "Compatibility in microstructural optimization for additive manufacturing," *Additive Manufacturing*, vol. 26, pp. 65–75, 2019.
- [38] J. Hu, M. Li, X. Yang, and S. Gao, "Cellular structure design based on free material optimization under connectivity control," *Computer-Aided Design*, vol. 127, p. 102854, 2020.
- [39] H. Zong, H. Liu, Q. Ma, Y. Tian, M. Zhou, and M. Y. Wang, "VCUT level set method for topology optimization of functionally graded cellular structures," *Computer Methods in Applied Mechanics and Engineering*, vol. 354, pp. 487–505, 2019.
- [40] X. Guo, W. Zhang, and W. Zhong, "Doing topology optimization explicitly and geometrically—a new moving morphable components based framework," *Journal of Applied Mechanics-Transactions of the ASME*, vol. 81, no. 8, 2014.
- [41] J. Panetta, Q. Zhou, L. Malomo, N. Pietroni, P. Cignoni, and D. Zorin, "Elastic textures for additive fabrication," *ACM Transactions on Graphics*, vol. 34, no. 4, pp. 135:1–12, 2015.
- [42] Z. Wu, L. Xia, S. Wang, and T. Shi, "Topology optimization of hierarchical lattice structures with substructuring," *Computer Methods in Applied Mechanics and Engineering*, vol. 345, pp. 602–617, 2019.
- [43] W. Wang, T. Y. Wang, Z. Yang, L. Liu, X. Tong, W. Tong, J. Deng, F. Chen, and X. Liu, "Cost-effective printing of 3D objects with skin-frame structures," *ACM Transactions on Graphics*, vol. 32, no. 6, pp. 177:1–10, 2013.
- [44] D. Li, W. Liao, N. Dai, and Y. Xie, "Anisotropic design and optimization of conformal gradient lattice structures," *Computer-Aided Design*, vol. 119, p. 102787, 2019.
- [45] C. Schumacher, S. Marschner, M. Cross, and B. Thomaszewski, "Mechanical characterization of structured sheet materials," *ACM Transactions on Graphics*, vol. 37, no. 4, pp. 148:1–15, 2018.
- [46] T. Tricard, V. Tavernier, C. Zanni, J. Martínez, P.-A. Hugron, F. Neyret, and S. Lefebvre, "Freely orientable microstructures for designing deformable 3D prints," *ACM Transactions on Graphics*, vol. 39, no. 6, pp. 211:1–16, 2020.
- [47] J. Hu, S. Wang, B. Li, F. Li, and L. Liu, "Efficient representation and optimization for TPMS-based porous structures," *IEEE Transactions on Visualization and Computer Graphics*, vol. 28, no. 7, pp. 2615–2627, 2022.
- [48] X. Yan, C. Rao, L. Lu, A. Sharf, H. Zhao, and B. Chen, "Strong 3D printing by TPMS injection," *IEEE Transactions on Visualization and Computer Graphics*, vol. 26, pp. 3037–3050, 2020.
- [49] D. C. Tozoni, J. Dumas, S. Jiang, J. Panetta, D. Panozzo, and D. Zorin, "A low-parametric rhombic microstructure family for irregular lattices," *ACM Transactions on Graphics*, vol. 39, no. 4, pp. 101:1–20, 2020.
- [50] D. Chen, M. Skouras, B. Zhu, and W. Matusik, "Computational discovery of extremal microstructure families," *Science Advances*, vol. 4, no. 1, p. 7005, 2018.
- [51] H. Wang, Y. Chen, and D. W. Rosen, "A hybrid geometric modeling method for large scale conformal cellular structures," in *ASME IDETC and CIE*, vol. 47403, 2005, pp. 421–427.
- [52] Q. Y. Hong and G. Elber, "Conformal microstructure synthesis in trimmed trivariate based V-Reps," *Computer-Aided Design*, vol. 140, p. 103085, 2021.
- [53] A. Gupta, K. Kurzeja, J. Rossignac, G. Allen, P. S. Kumar, and S. Musuvathy, "Programmed-lattice editor and accelerated processing of parametric program-representations of steady lattices," *Computer-Aided Design*, vol. 113, pp. 35–47, 2019.
- [54] M. Li, L. Zhu, J. Li, and K. Zhang, "Design optimization of inter-connected porous structures using extended triply periodic minimal surfaces," *Journal of Computational Physics*, vol. 425, p. 109909, 2020.
- [55] J. Ding, Q. Zou, S. Qu, P. Bartolo, X. Song, and C. C. Wang, "STL-free design and manufacturing paradigm for high-precision powder bed fusion," *CIRP Annals*, vol. 70, no. 1, pp. 167–170, 2021.

- [56] B. Liu, W. Cao, L. Zhang, K. Jiang, and P. Lu, "A design method of Voronoi porous structures with graded relative elasticity distribution for functionally gradient porous materials," *International Journal of Mechanics and Materials in Design*, vol. 17, pp. 863–883, 2021.
- [57] H. Liu, L. Chen, Y. Jiang, D. Zhu, Y. Zhou, and X. Wang, "Multi-scale optimization of additively manufactured graded non-stochastic and stochastic lattice structures," *Composite Structures*, vol. 305, p. 116546, 2023.
- [58] C. Zilber, "A globally convergent version of the method of moving asymptotes," *Structural Optimization*, vol. 6, no. 3, pp. 166–174, 1993.
- [59] W. Zhang, J. Yuan, J. Zhang, and X. Guo, "A new topology optimization approach based on moving morphable components (MMC) and the ersatz material model," *Structural and Multidisciplinary Optimization*, vol. 53, no. 6, pp. 1243–1260, 2016.
- [60] Q. Du, V. Faber, and M. Gunzburger, "Centroidal Voronoi tessellations: Applications and algorithms," *SIAM Review*, vol. 41, no. 4, pp. 637–676, 1999.
- [61] M. P. Bendsoe and O. Sigmund, *Topology Optimization: Theory, Methods and Applications*. Springer, 2003.
- [62] C. T. Loop and T. D. DeRose, "A multisided generalization of Bézier surfaces," *ACM Trans. on Graphics*, vol. 8, no. 3, pp. 204–234, 1989.
- [63] Z. Du, T. Cui, C. Liu, W. Zhang, Y. Guo, and X. Guo, "An efficient and easy-to-extend MATLAB code of the moving morphable component (MMC) method for three-dimensional topology optimization," *Structural and Multidisciplinary Optimization*, vol. 65, no. 158, 2022.
- [64] J. Gao, Z. Luo, L. Xia, and L. Gao, "Concurrent topology optimization of multiscale composite structures in MATLAB," *Structural and Multidisciplinary Optimization*, vol. 60, no. 6, pp. 2621–2651, 2019.
- [65] E. Andreassen, A. Clausen, M. Schevenels, B. S. Lazarov, and O. Sigmund, "Efficient topology optimization in MATLAB using 88 lines of code," *Structural and Multidisciplinary Optimization*, vol. 43, no. 1, pp. 1–16, 2011.
- [66] H. Xu, Y. Li, Y. Chen, and J. Barbič, "Interactive material design using model reduction," *ACM Transactions on Graphics*, vol. 34, no. 2, pp. 18:1–14, 2015.
- [67] D. Zhao, M. Li, and Y. Liu, "A novel application framework for self-supporting topology optimization," *The Visual Computer*, vol. 37, no. 5, pp. 1169–1184, 2021.
- [68] M.-J. Rakotosaona, N. Aigerman, N. J. Mitra, M. Ovsjanikov, and P. Guerrero, "Differentiable surface triangulation," *ACM Transactions on Graphics*, vol. 40, pp. 1–13, 2021.
- [69] P. Memari, P. Mullen, and M. Desbrun, "Parametrization of generalized primal-dual triangulations," in *International Meshing Roundtable Conference*, 2011.
- [70] B. Lévy and Y. Liu, "Lp centroidal Voronoi tessellation and its applications," *ACM Trans. on Graphics*, vol. 29, no. 4, pp. 119:1–11, 2010.
- [71] M. Budninskiy, B. Liu, F. de Goes, Y. Tong, P. Alliez, and M. Desbrun, "Optimal Voronoi tessellations with hessian-based anisotropy," *ACM Transactions on Graphics*, vol. 35, no. 6, pp. 1–12, 2016.
- [72] G. Fang, T. Zhang, S. Zhong, X. Chen, Z. Zhong, and C. C. L. Wang, "Reinforced FDM: Multi-axis filament alignment with controlled anisotropic strength," *ACM Transactions on Graphics*, vol. 39, no. 6, pp. 204:1–15, 2020.
- [73] D.-M. Yan, B. Levy, Y. Liu, F. Sun, and W. Wang, "Isotropic remeshing with fast and exact computation of restricted Voronoi diagram," *Computer Graphics Forum*, vol. 28, no. 5, pp. 1445–1454, 2009.



Ming Li is an associate professor at the State Key Laboratory of CAD&CG, Zhejiang University, China. He received his PhD degree in Applied Mathematics from the Chinese Academy of Sciences in 2004. From that on, he worked in Cardiff University, UK, and Drexel University, USA for four years. His research interest includes CAD/CAE integration, porous foams, and design optimization. Dr. Li has published more than 50 peer-reviewed international papers on the topics.



Jingqiao Hu received the PhD degree in Computer Science from Zhejiang University, China, in 2022. Her research interests include numerical coarsening and topology optimization.



Wei Chen received the bachelor's degree in Computer Science from Lanzhou University, China, in 2021. He is now a PhD student in the State Key Laboratory of CAD&CG, Zhejiang University. His research interests include physical simulation and computer-aided design.



Weipeng Kong received the Master's degree in Computer Science from Zhejiang University, China, in 2023. His research interests include computer graphics and architectures of CAD system.



Jin Huang is a professor in the State Key Lab of CAD&CG of Zhejiang University, China. He received his Ph.D. degree in Computer Science Department from Zhejiang University in 2007 with Excellent Doctoral Dissertation Award of China Computer Federation. His research interests include geometry processing and physically-based simulation. He has served as reviewer for ACM SIGGRAPH, EuroGraphics, Pacific Graphics, TVCG etc.